T-matrix method for acoustical Bessel beam scattering from a rigid finite cylinder with spheroidal endcaps

Zhixiong Gong[a], Wei Li[a,b,c,*], Yingbin Chai[a], Yao Zhao[a,b,c], Farid G. Mitri[d]

[a] School of Naval Architecture and Ocean Engineering, Huazhong University of Science and Technology, Wuhan 430074, PR China
[b] Hubei Key Laboratory of Naval Architecture and Ocean Engineering Hydrodynamics (HUST),Wuhan 430074, PR China
[c] Collaborative Innovation Center for Advanced Ship and Deep-Sea Exploration (CISSE),Shanghai 200240, PR China
[d] Chevron, Area 52 Technology–ETC, Santa Fe, New Mexico 87508, USA

ARTICLE INFO

ABSTRACT

In this paper, the T-matrix (null-field) method is developed to investigate the acoustic scattering by a rigid fixed (immovable) finite cylinder with two spheroidal endcaps immersed in a non-viscous fluid under the illumination of an unbounded zeroth-order Bessel beam with arbitrary orientation. Based on the proposed method, a MATLAB software package is constructed accordingly, and then verified and validated to compute the acoustic scattering by a rigid finite-length cylinder in the Bessel beam. Several numerical examples are carried out to investigate the novel phenomenon of acoustic scattering by a cylinder with spheroidal endcaps in a Bessel beam with arbitrary incidence, with particular emphasis on the aspect ratios (including the ratio of total length to diameter of the finite cylinder and the ratio of polar radius to equatorial radius of the spheroidal endcaps), the half-cone angle of Bessel beam, the dimensionless frequency, as well as the angle of incidence. The quasi-periodic oscillations are observed in the plots of the far-field backscattering form function modulus versus the dimensionless frequency, owing to the interference between the specular reflection and the Franz wave circumnavigating the finite cylinder in the surrounding fluid. A geometrical model of Bessel beam scattering is employed to further verify the effectiveness of the T-matrix method. Furthermore, the 3D far-field scattering directivity patterns at end-on incidence and 2D polar plots at arbitrary angles of incidence are exhibited, which could provide new insights into the physical mechanisms of Bessel beam scattering by finite cylinders with spheroidal endcaps of different aspect-ratios. This research work provides an impetus for engineering applications in underwater acoustics, particle characterization and the interaction of elongated structures with acoustical Bessel beams.

1. Introduction

Over the past decades, there has been considerable interest in the study of acoustic scattering off finite-length cylinders in underwater environments. This is because the cylinder with finite length is sometimes quite appropriate to model many finite size objects in the ocean occurring in nature (such as plankton, fish, rock, etc.) and engineering applications (such as submarine, torpedo). Note that exact solutions are available for the scattering of acoustic waves from objects with simple geometry shapes, such as the infinitely long cylinder and sphere (Rayleigh, 1945; Faran, 1951; Lax and Feshbach, 1948; Hickling, 1958; Anderson, 1950; Gaunaurd and Überall, 1983), but those seem either impossible or extremely difficult to obtain in closed-form compact expressions for the case of finite cylinder. To overcome the lack of the exact analytical solutions, semi-analytical and numerical

methods were accordingly developed to investigate the acoustic scattering by a cylinder with a finite length. A number of useful methods were proposed and verified, including the T-matrix (null-field) method (Waterman, 1969), the boundary integral method (Schenck, 1968), the Kirchhoff approximate method (Gaunaurd, 1985), the geometric theory of diffraction (GTD) (Keller and Ahluwalia, 1971), the Sommerfeld-Watson transformation (Rumerman, 1992), the matched asymptotic expansions method (Van Nhieu and Ywanne, 1994), an asymptotic method based on partial-wave series (Junger, 1982; Stanton, 1988) that was improved by means of the Kirchhoff integral theorem (Ye, 1997), and the Freedman's approach (Freedman, 1962; Narayanan and Garg, 1968). Because of its superior properties, such as accuracy and high computational efficiency, the T-matrix approach is a competitive tool to investigate the acoustic scattering characteristics of the submerged cylinder of finite length comparing with the other (approx-

imate) methods.

The *T*-matrix method (Waterman, 1969, 1965) has been demonstrated to be very effective to deal with scattering problems for a variety of targets with different shapes, including spheres (Peterson and Ström, 1974; Jansson, 1993; Liu et al., 2016), cylinders (Varadan, 1978; Hackman and Todoroff, 1985; Su et al., 1980), spheroids (Varadan et al., 1982; Green, 1987), and so on. Besides the acoustic scattering, the *T*-matrix method can be also extended to compute the scattering of electromagnetic and elastodynamic fields (Varadan and yaradan, 1980; Varadan and Varadan, 1987). The advantage of the *T*-matrix method is to expand all field quantities in terms of a set of spherical functions, which is convenient from a computational standpoint. The main point of the present method is to obtain the *T* matrix (transition matrix) that gives a direct relationship between the known expansion coefficients of the incident waves and the unknown expansion coefficients of the scattered field. Furthermore, the *T*-matrix formulation can be extended for the computation of the scattering from complex combination of objects, the spherically end-capped circle cylinder for instance, and other geometries, only by changing the surface shape function of the considered target accordingly. Therefore, there is obvious evidence that the *T*-matrix method can be implemented to calculate the acoustic scattering from a finite cylinder with hemispheroidal endcaps as long as the expressions of surface are known and given explicitly.

Unfortunately, the above-mentioned works have mainly considered the case of infinite plane wave incidence. There is a need to extend the *T*-matrix method to study the scattering characteristics from targets in actual *beams* since they have recently attracted increasing attention from many researchers in various fields (optics, electromagnetics, acoustics, fluid dynamics, etc.), and seem to be very promising in engineering practices. Bessel beams, are one kind of the undistorted waves, that possess several advantages over infinite plane waves and Gaussian beams, because they can propagate without distortion over a characteristic distance in free space. In addition, a Bessel beam is characterized by two important features, namely, the non-diffraction property and self-construction ability. The former feature means that the transverse intensity profile in the plane perpendicular to the direction of Bessel beam axis remains unaltered (Durnin et al., 1987; Piestun and Shamir, 1998; Bouchal, 2003; López-Mariscal and Gutiérrez-Vega, 2007), while the second one describes the ability of the Bessel beam to reconstruct its initial intensity profile after encountering an obstacle in the case where the incident waves (forming the beam) are not blocked completely (Bouchal et al., 1998; Garces-Chavez et al., 2002; Fahrbach et al., 2010).

To date, however, the study on acoustical Bessel beams is somewhat limited, especially on the issue of acoustic scattering for complex targets, and thus more attention should be paid to this aspect. As reported in the previous works, most were mainly focused on scatterers with spherical (Marston, 2006, 2007a, 2007b, 2007c, 2008, 2009; Zhang and Marston, 2011, 2012; Mitri, 2008a, 2008b, 2009a, 2009b, 2009c, 2011; Mitri and Fellah, 2011; Mitri and Silva, 2011; Silva, 2011; Silva et al., 2013) and recently spheroidal shapes. Meanwhile, extensive efforts have been undertaken to explore the acoustical scattering characteristics by spherical shell (Marston, 2007a, 2007b, 2008; Mitri, 2010) and rigid spheroid (Marston et al., 2006; Mitri, 2015a, 2015b, 2015c), in either zeroth or high order Bessel beam illumination. Moreover, the acoustical Bessel beam scattering from rigid spheroid and finite cylinder with two hemispherical endcaps was briefly investigated using the *T*-matrix method (Li and Li, 2012; Li et al., 2015). To the best of the authors' knowledge, the acoustic scattering by a rigid finite cylinder with spheroidal endcaps immersed in a non-viscous fluid under the illumination of an unbounded Bessel beam has not been reported in the existing literature, and still remains an unsolved problem. In the present paper, the *T*-matrix method is further developed to explore the novel phenomenon of Bessel beam scattering by the combination of a rigid finite cylinder with two

spheroidal endcaps immersed in the surrounding fluid, and this can provide some novel insights into the scattering mechanisms of acoustical Bessel beams interacting with underwater objects of complex shapes.

The frame of this article is outlined as follows. In Section 2.1, the necessary theoretical formulation of the *T*-matrix method for the acoustic scattering by the rigid spheroidally-endcapped finite cylinder immersed in fluid are presented. Subsequently, the structure of the *Q*-matrix (used to build the *T*-matrix) is presented, and several simplifying methods are given explicitly in Section 2.2 for the case where the shape of the target has a symmetry property. Section 2.3 gives a detailed derivation of the expansion coefficients of the incident Bessel beam with arbitrary incidence. In Section 3.1, numerical validation is firstly implemented to verify the correctness of the *T*-matrix approach for finite cylinders with spherical endcaps. Meanwhile, the convergence tests are also carried out. Additional numerical examples are performed with particular emphasis on the aspect ratios (including the ratio of total length to diameter of the finite cylinder and the ratio of polar radius to equatorial radius of the spheroidal endcaps), the half-cone angles, the dimensionless frequency, as well as the incidence angles of the Bessel beam. The geometric model is also implemented to interpret the physical mechanism of the oscillations in the back-scattering form function curves. Finally, some useful concluding remarks and future work are summarized in Section 4.

2. Theoretical method

In this part, the necessary formulas of the *T*-matrix method for acoustic scattering by a rigid finite cylinder with two spheroidal endcaps immersed in fluid under Bessel wave incidence are presented. In the following, the structure of the *Q*-matrix is described in detail and several simplifying methods are illustrated. Finally, the detailed procedure for deriving the expansion coefficients for an incident unbounded zeroth-order Bessel beam is also provided.

2.1. T-matrix method for a rigid finite cylinder in a non-viscous fluid

Consider a rigid finite cylinder with two spheroidal endcaps immersed in an infinite, homogeneous and nonviscous fluid under the illumination of an acoustic monochromatic zeroth-order Bessel beam at an arbitrary angle of incidence θ_i. In the computations, the incident azimuthal angle is chosen such that $\varphi_i = 0°$. Panel (a) of Fig. 1 describes the end-on incidence case ($\theta_i = 0°$), while panel (b) describe the oblique incidence case ($0° < \theta_i < 90°$), respectively. The geometrical parameters of the finite-length cylinder are shown in Fig. 1, with the half length of the cylindrical portion h, the radius of the cylinder b, and the polar radius of the spheroidal endcap d. The half-length of the finite cylinder with spheroidal endcaps is therefore $l = h + d$. The ideal fluid surrounding the cylinder has a sound velocity c and a density ρ. For convenience, the time-dependence of all fields [which is of the form $\exp(-i\omega t)$] is suppressed for convenience since all fields have the same harmonic time-dependency.

The total velocity potential $\phi(\mathbf{r})$ in the surrounding fluid is written as the sum of the incident $\phi^i(\mathbf{r})$ and the scattered $\phi^s(\mathbf{r})$ velocity potentials:

$$\phi(\mathbf{r}) = \phi^i(\mathbf{r}) + \phi^s(\mathbf{r}) \tag{1}$$

Note that all the above velocity potentials satisfy the scalar Helmholtz equations which can be expressed as

$$(\nabla^2 + k^2) \begin{pmatrix} \phi(\mathbf{r}) \\ \phi^i(\mathbf{r}) \\ \phi^s(\mathbf{r}) \end{pmatrix} = 0 \tag{2}$$

where $k = \omega/c$ is the wave number in the surrounding fluid and ω is the angular frequency. In the following, the integral representation and the

(a)

Zeroth-order Bessel beam

Rigid finite cylinder with
spheroidal endcaps

(b)

Zeroth-order Bessel beam

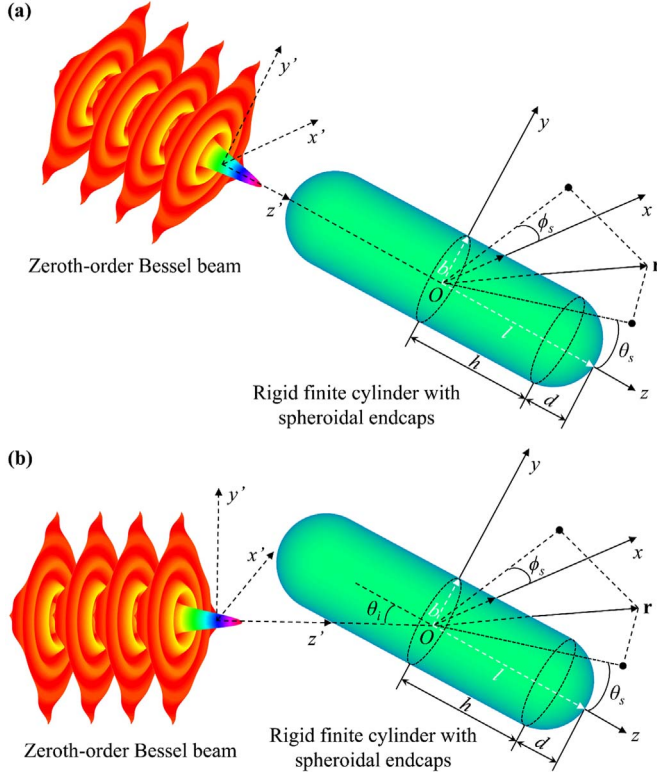Rigid finite cylinder with
spheroidal endcaps

Fig. 1. The schematic of a monochromatic zeroth-order Bessel beam interacting with a rigid fixed (immovable) cylinder with spheroidal endcaps for end-on ($\theta_i = 0°$) incidence (panel (a)) and oblique ($0° < \theta_i < 90°$) incidence (panel (b)) in a spherical coordinates system.

null field equation, which are originally presented in (Waterman, 1969) are given by

$$\phi^i(\mathbf{r}) + \int_S [\phi_+ \overrightarrow{\mathbf{n}} \cdot \nabla g(\mathbf{r}, \mathbf{r}') - (\overrightarrow{\mathbf{n}} \cdot \nabla_+ \phi) g(\mathbf{r}, \mathbf{r}')] \mathrm{d}S = \begin{cases} \phi(\mathbf{r}) & \mathbf{r} \text{ outside } S \\ 0 & \mathbf{r} \text{ inside } S \end{cases} \tag{3}$$

where

$$g(\mathbf{r}, \mathbf{r}') = \exp(ik|\mathbf{r} - \mathbf{r}'|)/(k|\mathbf{r} - \mathbf{r}'|) \tag{4}$$

is the free space Green's function of the Helmholtz equation. S represents the surface of the finite cylinder with spheroidal endcaps and $\overrightarrow{\mathbf{n}}$ is the unit normal pointing outwardly. The quantities ϕ_+ and $\overrightarrow{\mathbf{n}} \cdot \nabla_+ \phi$ stand for the velocity potential and normal component of the velocity on the outside of S, respectively.

The spheroidally-endcapped cylinder of finite length considered here is assumed to be perfectly rigid. Because of an azimuthal symmetry, the surface shape function of cylinder $r(\theta)$ is only dependent on the polar angle θ, with its representation as follow

$$r(\theta) = \begin{cases} b/\sqrt{1 - x^2}, & \text{if } 0 \le x \le \alpha \\ s(x) & \text{if } \alpha \le x \le 1 \end{cases} \tag{5}$$

where s is a function of the endcap shape, and x and α are given below, respectively.

$$x = \cos \theta \tag{6}$$

$$\alpha = h/\sqrt{h^2 + b^2} \tag{7}$$

where α is the critical cosine value when the point on the surface $r(\theta)$ moves from the cylindrical section to the endcap.

For the perfectly rigid finite cylinder, the Neumann boundary condition is imposed on the surface of the spheroid at $r = r(\theta)$ such that

$$\overrightarrow{\mathbf{n}} \cdot \nabla_+ \phi(\mathbf{r})|_{r=r(\theta)} = 0 \tag{8}$$

In order to obtain the T-matrix for the rigid cylinder of finite length, all three fields in Eq. (2) and the Green's function should be expanded in terms of a set of spherical harmonic functions. To this end, the following scalar basis function is defined as

$$\phi_{nm\sigma}(\mathbf{r}) = \xi_{nm} h_n(kr) P_n^m(\cos \theta) \begin{pmatrix} \cos(m\varphi), & \sigma = e \\ \sin(m\varphi), & \sigma = o \end{pmatrix} \tag{9}$$

where,

$$\xi_{nm} = \left(\varepsilon_m \frac{(2n + 1)(n - m)!}{4\pi(n + m)!} \right)^{1/2} \tag{10}$$

and $h_n(kr)$ is the spherical Hankel function of the first kind, $P_n^m(\cos \theta)$ are the associated Legendre functions and $\varepsilon_m = 2 - \delta_{m0}$ is the Neumann factor. $\sigma = e$, o (even, odd) specifies the azimuthal parity, $m = 0, 1, ..., n$ specifies the rank, and $n = 0, 1, ..., \infty$ specifies the order of the spherical wave functions.

Due to the fact that the incident fields are finite at the origin, the spherical Hankel function of the first kind (which is singular at the origin) in Eq. (9) should be replaced by the spherical Bessel function of the first kind $j_n(kr)$ which is regular at the origin. Therefore, we can use the revised basis function, denoted by $\mathrm{Re}\{\phi_{nm\sigma}\}$, to expand the *incident* field.

The velocity potentials of the incident and scattered fields can be expanded as

$$\phi^i(\mathbf{r}) = \sum_{n=0}^{\infty} \sum_{m=0}^{n} \sum_{\sigma} a_{nm\sigma} \mathrm{Re}\{\phi_{nm\sigma}(\mathbf{r})\} \tag{11}$$

$$\phi^s(\mathbf{r}) = \sum_{n=0}^{\infty} \sum_{m=0}^{n} \sum_{\sigma} f_{nm\sigma} \phi_{nm\sigma}(\mathbf{r}) \tag{12}$$

where $a_{nm\sigma}$ are the known coefficients of the incident Bessel beam (derived in Section 2.3) and $f_{nm\sigma}$ are the unknown coefficients of the scattered fields, respectively. Note that the infinite summation in Eqs. (11) and (12) cannot be evaluated practically. Nevertheless, they can be numerically computed after adequate truncation at an appropriate limit $n_{\max}$. Preferably, the maximum truncations limits could be continually increased until adequate convergence and negligible numerical error are ensured (see Fig. 3). Noticeably, to make a compromise by the computational cost and the stability of the matrix inversion procedures, this limit should be judiciously chosen so that high precision and adequate convergence of the truncated series are warranted and the computational cost could be satisfied.

In addition, the Green's function $g(\mathbf{r}, \mathbf{r}')$ and the unknown surface field ϕ_+ are also expanded in the following forms

$$g(\mathbf{r}, \mathbf{r}') = ik \sum_n \sum_m \sum_\sigma \phi_{nm\sigma}(r_>) \mathrm{Re}\{\phi_{nm\sigma}(r_<)\} \tag{13}$$

$$\phi_+(\mathbf{r}) = \sum_n \sum_m \sum_\sigma \alpha_{nm\sigma} \phi_{nm\sigma}(\mathbf{r}) \tag{14}$$

Up to now, all the necessary formulas, including the integral representations, the rigid boundary condition and expansions of all fields and Green's function, have been obtained, and hence, the T-matrix can be derived immediately in an obvious matrix notation as

$$f = Ta \tag{15}$$

where T is the transition matrix (T-matrix) of rigid finite cylinder with spheroidal endcaps given by

$$T = -Q^{-1} \mathrm{Re}\{Q\} \tag{16}$$

with the expression of the elements in Q given as follows

$$Q_{nm,n'm'}^{\sigma\sigma'} = \int_S \mathrm{Re}\, \phi_{n'm'\sigma'} \overrightarrow{\mathbf{n}} \cdot \nabla \phi_{nm\sigma} \mathrm{d}S \tag{17}$$

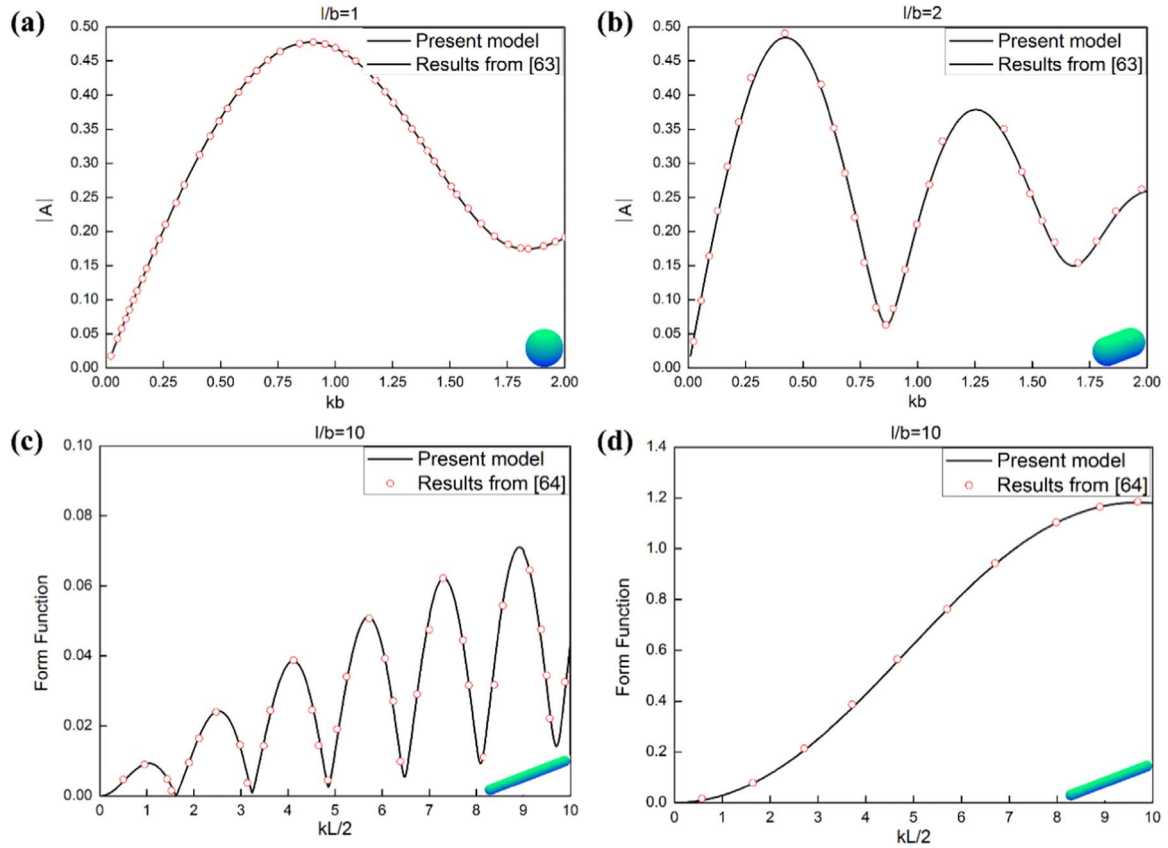It can be noted that in Eq. (15), the transition matrix gives a direct

Fig. 2. Panels (a) and (b) describe the far-field backscattering amplitude |A| corresponding to a rigid fixed (immovable) cylinder with spherical endcaps ($d = b$) with an aspect ratio of $l/b = 1$ (the sphere case) and $l/b = 2$, respectively, for end-on ($\theta_i = 0°$) incidence. Panels (c) and (d) describe the far-field backscattering form function modulus for a rigid fixed (immovable) cylinder with spherical endcaps with $l/b = 10$ for end-on ($\theta_i = 0°$) and broadside ($\theta_i = 90°$) incidence, respectively. The solid lines are computed using the *T*-matrix method presented here, while the circles correspond to the numerical calculations obtained from the same method, given in Fig. 4 of Sarkissian et al. (1993) corresponding to panels (a) and (b), and Fig. 18 (A) of (Hackman, 1993) corresponding to panels (c) and (d), respectively.

relationship between the known expansion coefficients of the incident waves and the unknown expansion coefficients of the scattered field. Moreover, as observed from Eqs. (16) and (17), the transition matrix is independent of the source, and solely depends on the frequency of the incident waves, the geometry of the scatterer and the corresponding boundary conditions at the interface.

2.2. Structure of the Q matrix and simplifying methods

To further understand the foregoing matrix equations, the structure of the Q matrix will be discussed in detail and several simplifying methods are also presented in the case where the object considered has a geometrical symmetry. In Eq. (17), the indices of the elements in Q are denoted by ($nm\sigma$, $n'm'\sigma'$), and it is noticeably convenient to break the Q matrix into four blocks according to the azimuthal parity as expressed as follows

$$Q = \begin{bmatrix} Q^{ee} & Q^{eo} \\ Q^{oe} & Q^{oo} \end{bmatrix} \tag{18}$$

For each block in Eq. (18), it should be noted that the indices, for either even or odd parity, are

$$\begin{array}{lll} n = 0, 1, \ldots, \infty; & m = 0, 1, \ldots, n; & \sigma = e; \\ n = 0, 1, \ldots, \infty; & m = 1, 2, \ldots, n; & \sigma = o; \end{array} \tag{19}$$

Notice that the index n cannot approach infinity (∞) from a computational standpoint in practice, and thus, it must be truncated at an appropriate limit n_{max}, as briefly discussed in Section 2.1. In order to present the structure of the Q-matrix conveniently, in general, a rule is to set the truncation limit as $n_{max} = 6 + \text{Int}(ka)$ (Varadan et al.,

1991), with the ka being the dimensionless frequency. Consider an arbitrary block in the Q-matrix, for example Q^{ee}. The detailed form of (nm, $n'm'$) in Q^{ee} when $n = n' = 2$ can be written explicitly as follows

$$\begin{bmatrix} (00, 00) & (00, 10) & (00, 11) & (00, 20) & (00, 21) & (00, 22) \\ (10, 00) & (10, 10) & (10, 11) & (10, 20) & (10, 21) & (10, 22) \\ (11, 00) & (11, 10) & (11, 11) & (11, 20) & (11, 21) & (11, 22) \\ (20, 00) & (20, 10) & (20, 11) & (20, 20) & (20, 21) & (20, 22) \\ (21, 00) & (21, 10) & (21, 11) & (21, 20) & (21, 21) & (21, 22) \\ (22, 00) & (22, 10) & (22, 11) & (22, 20) & (22, 21) & (22, 22) \end{bmatrix} \tag{20}$$

Similarly, the forms of (nm, $n'm'$) for Q^{eo}, Q^{oe} and Q^{oo} can be acquired at the same transition limit ($n = n' = 2$). Consequently, the total size of the Q matrix, including four blocks, can be summed up as $(n_{max} + 1)^2 \times (n_{max} + 1)^2$. In the low-frequency bandwidth, typically for $ka < 1$ to the maximum truncation index is $n_{max} = 7$ and thus the size of the Q matrix is 64×64. It is noteworthy that each element in the Q-matrix requires computation of the quadric integral involving mixed products of Bessel and Legendre functions on the surface of obstacle, leading to the complexity and a high computational cost to solve the Q-matrix of large size. Nevertheless, the geometry symmetry of the object will dramatically reduce the computational cost of the Q-matrix using several simplifying methods.

In the spherical coordinates, the integral expression of the element in the Q-matrix in Eq. (17) turns into

$$Q^{\sigma\sigma'}_{nm,n'm'} = \int_0^\pi \int_0^{2\pi} \text{Re}\, \phi_{n'm'\sigma'} \overrightarrow{\mathbf{n}} \cdot \nabla \phi_{nm\sigma} r^2 \sin\theta\, d\varphi\, d\theta \tag{21}$$

For an obstacle possessing an axis of rotational symmetry, in the case where the origin of the coordinates is put in the interior of the
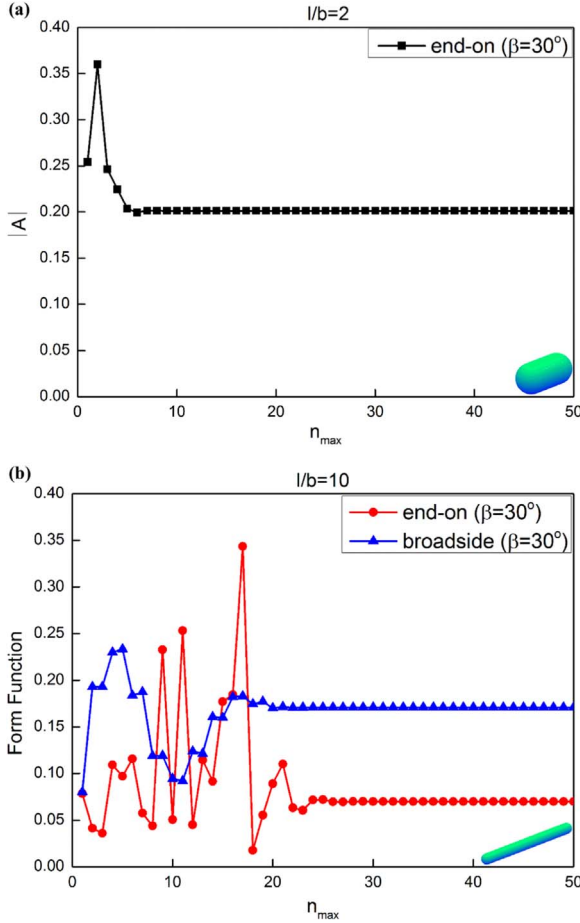
Fig. 3. Panel (a) corresponds to the far-field backscattering amplitude $|A|$ for a rigid fixed (immovable) cylinder with spherical endcaps ($d = b$) having an aspect ratio $l/b = 2$ for $kb = 2$ for end-on ($\theta_i = 0°$) incidence as a function of the maximum truncation index n_{max}. Panel (b) corresponds to the far-field backscattering form function modulus for a rigid fixed (immovable) cylinder with spherical endcaps with $l/b = 10$ for $kL/2 = 10$ for end-on ($\theta_i = 0°$) and broadside ($\theta_i = 90°$) incidence, respectively, as a function of the maximum truncation index n_{max}. In these cases, the half-cone angle is set to $\beta = 30°$.

obstacle and at the center of the symmetry axis, the surface shape function only depends on the polar angle θ, and is independent of the azimuthal angle φ (i.e. $r_\varphi = \frac{\partial r(\theta)}{\partial \varphi} = 0$). Thus, the following equation can be obtained

$$\vec{\mathbf{n}} \cdot \nabla \phi_{nm\sigma} = \frac{\partial \phi}{\partial r} + \frac{r_\theta}{r^2} \frac{\partial \phi}{\partial \theta} \tag{22}$$

where r_θ represents the partial derivative of $r(\theta)$ with respect to the polar angle θ. Substituting Eqs. (9), (10) and (22) into Eq. (21) yields

$$Q_{nm,n'm'}^{\sigma\sigma'} = \int_0^\pi \xi_{n'm'} j_{n'}(kr) P_{n'}^{m'}(\cos\theta) \xi_{nm}$$
$$\left[\frac{\partial h_n(kr)}{\partial r} P_n^m(\cos\theta) - \frac{r_\theta}{r^2} h_n(kr) \frac{\partial P_n^m(\cos\theta)}{\partial \theta} \right] \times$$
$$r^2 \sin\theta d\theta \int_0^{2\pi} \begin{pmatrix} \cos m'\varphi \\ \sin m'\varphi \end{pmatrix} \begin{pmatrix} \cos m\varphi \\ \sin m\varphi \end{pmatrix} d\varphi \tag{23}$$

As observed from Eq. (23), several simplifications can be utilized for an object with rotational symmetry, such that: (i) $Q_{nm,n'm'}^{eo} = Q_{nm,n'm'}^{oe} = 0$; (ii) $Q_{nm,n'm'}^{ee} = Q_{nm,n'm'}^{oo} = 0$ when $m \neq m'$; (iii) $Q_{nm,n'm'}^{ee} = Q_{nm,n'm'}^{oo}$ with the exception of $m = 0$ or $m' = 0$. As a result, significant reduction of the computational cost for the elements of Q matrix can be achieved by introducing the simplifying methods, and only the following elements in the block $Q_{nm,n'm'}^{ee}$ need to be calculated. Namely,

$$Q_{nm,n'm'}^{ee} = \beta_m \xi_{n'm'} \xi_{nm} \int_0^\pi j_{n'}(kr) P_{n'}^{m'}(\cos\theta)$$
$$\left[\frac{\partial h_n(kr)}{\partial r} P_n^m(\cos\theta) - \frac{r_\theta}{r^2} h_n(kr) \frac{\partial P_n^m(\cos\theta)}{\partial \theta} \right]$$
$$\times r^2 \sin\theta d\theta \tag{24}$$

where

$$\beta_m = \begin{cases} \pi, & m \neq 0 \\ 2\pi, & m = 0 \end{cases} \tag{25}$$

Furthermore, it is possible to make additional reductions if the object has the mirror symmetry at the same time, and we only need to compute the matrix elements with the following indices when $(n + n')$ is even. Meanwhile, the integration range can be reduced to $0 < \theta < \pi/2$. Finally, the transition matrix will benefit from the above simplifying method in computational efficiency (see Eq. (16)).

2.3. Expansion coefficients of the incident Bessel beam

In this part, the expressions for the expansion coefficients $a_{nm\sigma}$ in the case of a zeroth-order Bessel beam are derived. Once the expansion coefficients of the incident Bessel beam are obtained, they can be utilized to calculate the acoustic scattered fields using the *T*-matrix method accordingly. Our motivation is to expand the velocity potential of the zeroth-order Bessel beam into two parts in a product form, namely the revised basis function $\text{Re}\{\phi_{nm\sigma}(\mathbf{r})\}$ and the desired incident coefficients of Bessel beam $a_{nm\sigma}$.

The starting point of derivation begins with an expansion expression of the complex velocity potential of an unbounded zeroth-order Bessel beam. According to Eq. (B2) in Appendix B (Marston, 2007a), the complex velocity potential of the zeroth-order Bessel beam $\phi_{ZOBB}^{(inc)}(r, \theta)$ can be expanded in spherical coordinates (r, θ, φ) as follows, (with the time factor $\exp(-i\omega t)$ being left out)

$$\phi_{ZOBB}^{(inc)} = \phi_0 \sum_{n=0}^{\infty} i^n (2n + 1) j_n(kr) P_n(\cos\theta) P_n(\cos\beta) \tag{26}$$

where ϕ_0 is the beam amplitude, β denotes the half-cone angle of the Bessel beam and θ is the polar angle. By using the addition theorem for the Legendre functions (Stratton, 2007), the expression for $P_n(\cos\theta)$ becomes

$$P_n(\cos\theta) = \sum_{m=0}^{n} \varepsilon_m \frac{(n-m)!}{(n+m)!} P_n^m(\cos\theta_i) P_n^m(\cos\theta_s) \cos m(\varphi_i - \varphi_s) \tag{27}$$

where θ_i and θ_s represent the incident and scattered axial angles, respectively.

Substituting Eqs. (9), (10), (27) into Eq. (26), the complex velocity potential of the zeroth-order Bessel beam is expressed according to a product form as

$$\phi_{ZOBB}^{(inc)} = a_{nm\sigma} \text{Re}\{\phi_{nm\sigma}(\mathbf{r})\} \tag{28}$$

where $a_{nm\sigma}$ stands for the expansion coefficients of the incident unbounded zeroth-order Bessel beam given by (Li and Li, 2012)

$$a_{nm\sigma} = 4\pi \xi_{nm} i^n P_n^m(\cos\theta_i) P_n^m(\cos\beta) \begin{pmatrix} \cos(m\varphi_i), & \sigma = e \\ \sin(m\varphi_i), & \sigma = o \end{pmatrix} \tag{29}$$

It should be noted that the expression of the expansion coefficients depends on the half-cone angle β, as well as the incident axial angles θ_i and azimuthal angles φ_i. The half-cone angle β is a characteristic parameter of the Bessel beam, which is in fact the angle describing the plane wave vector component with respect to the beam axis. Particularly, when $\beta = 0°$, the zeroth-order Bessel beam turns into the standard plane wave. The incident axial angle θ_i can vary from $0°$ to $360°$.

After substituting Eq. (14) and the expansion coefficients for the incident Bessel beam given by Eq. (29) into the relationship according
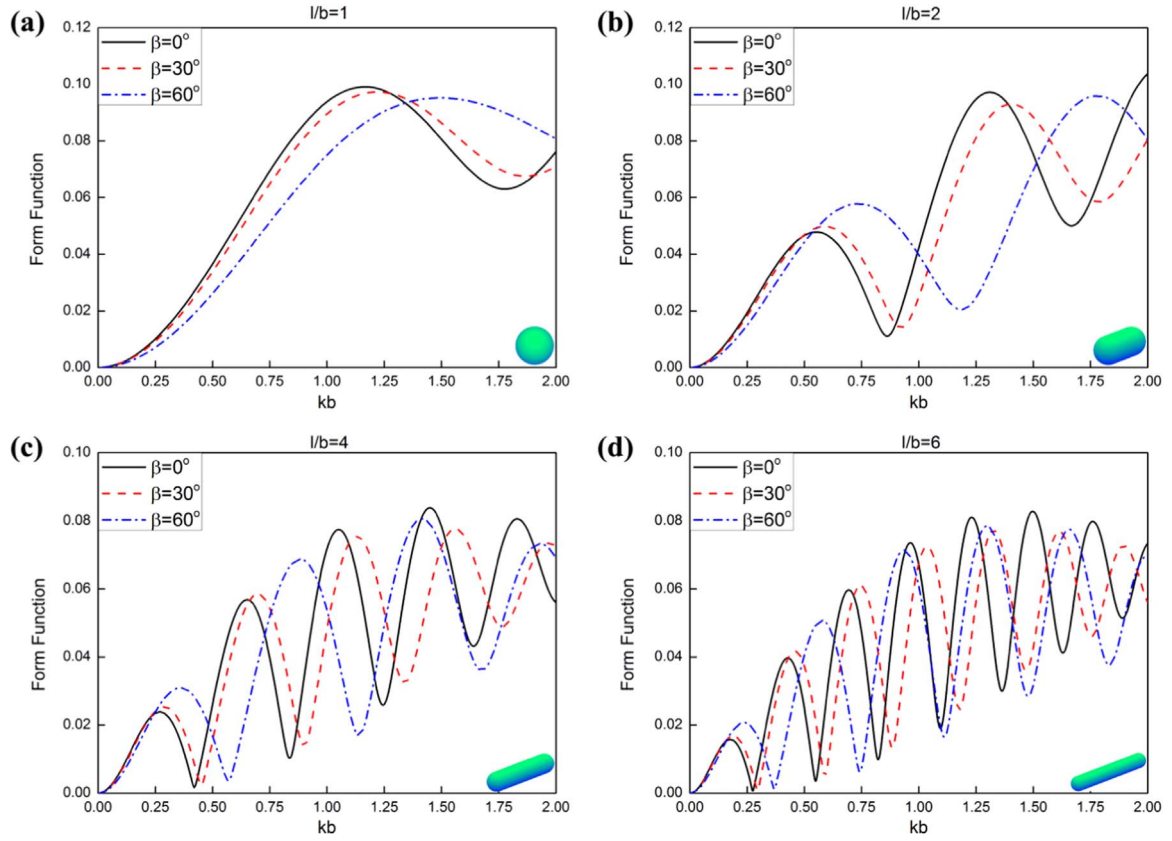
Fig. 4. The far-field backscattering form function modulus at end-on incidence $\theta_i = 0°$ with different half-cone angles β of the Bessel beam versus the dimensionless frequency for a rigid fixed (immovable) cylinder with spherical endcaps ($d = b$). Panels (a)–(d) correspond to aspect ratio of $l/b = 1, 2, 4$ and 6, respectively. The case where $\beta = 0°$ corresponds to infinite plane waves.
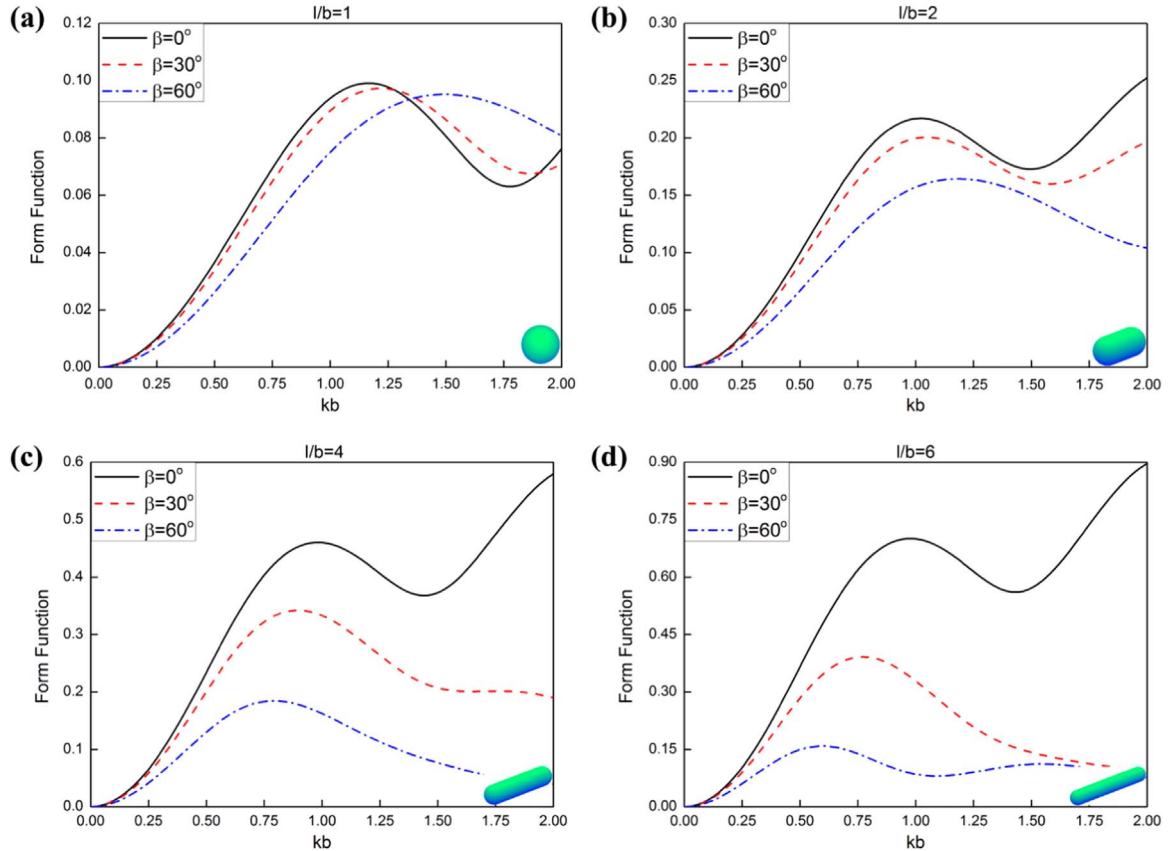

Fig. 5. The same as in Fig. 4, but the plots correspond to the broadside ($\theta_i = 90°$) incidence case.
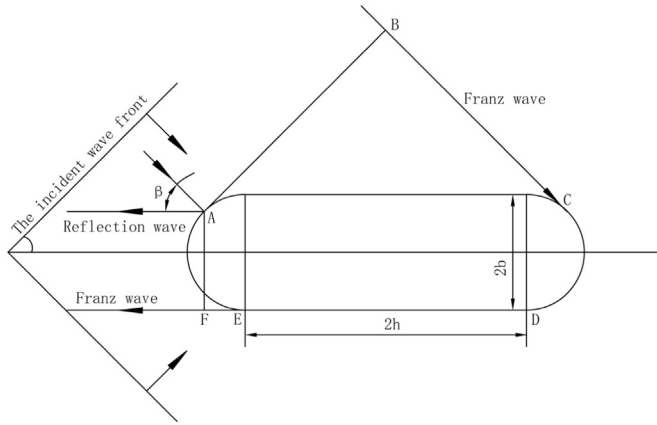
Fig. 6. The sketch of the geometrical model using rays in the description of the Bessel beam scattering by a rigid fixed (immovable) cylinder with spherical endcaps $(d = b)$ for end-on incidence $\theta_i = 0°$, with the half-cone angle β.

Table 1
Comparison of the peak-to-peak intervals of the far-field backscattering form function modulus versus the dimensionless frequency for a rigid fixed (immovable) cylinder with spherical endcaps $(d = b)$ with four values of the aspect ratios $l/b = 1$, 2, 4, 6, respectively, corresponding to half-cone angles $\beta = 0°$, 30°, 60°.

Aspect ratio l/b	Half-cone angle β	Predicted by geometrical model	Obtained from Fig. 4
1	0°	1.22	1.21
	30°	1.38	1.37
	60°	1.64	1.64
2	0°	0.69	0.75
	30°	0.76	0.81
	60°	0.92	1.04
4	0°	0.37	0.39
	30°	0.40	0.42
	60°	0.49	0.52
6	0°	0.25	0.26
	30°	0.27	0.28
	60°	0.33	0.35

to Eq. (15), the corresponding scattered fields by a rigid finite cylinder with spheroidal endcaps under the illumination of an ideal zeroth-order Bessel beam can be acquired at once by Eq. (12). Using the asymptotic form of the spherical Hankel function, the far-field velocity potential could be written in the form of f_∞ as

$$\lim_{r \to \infty} \phi^s = \phi_0 \frac{b}{2r} f_\infty(kr_0, \theta, \varphi, \beta)\exp(ikr) \tag{30}$$

where b is the radius of the finite-length cylinder and keeps constant for rigid finite cylinders with different aspect ratios. The parameter r is the distance from the origin to the field point. In addition, the form function f_∞ gives the angular variation of the scattered far field.

3. Numerical results and discussions

A MATLAB software package is developed according to the foregoing analytical methods to calculate the far-field scattering by a rigid finite cylinder with two spheroidal endcaps illuminated by an ideal zeroth-order Bessel beam. Several numerical techniques are implemented to obtain the Q-matrix. Specifically, the elements of the Q-matrix are obtained by Gauss-Legendre quadrature algebraic manipulations by using appropriate equations to describe the surfaces of the objects. In addition, the inversion procedure of the Q-matrix is conducted throughout the Gaussian elimination procedure straightforwardly. A number of numerical examples are carried out to demonstrate the feasibility of utilizing the T-matrix method to compute the acoustic scattering of an ideal zeroth-order Bessel beam by a rigid

finite-length cylinder.

3.1. Numerical verification and validation

To verify the accuracy of the theoretical formulas based on the T-matrix method presented above for the Bessel beam, several numerical examples aiming to obtain the far-field backscattering fields by a rigid finite cylinder with spherical endcaps (for convenience, $d = b$ in Fig. 1), were conducted, and the corresponding comparisons were made with previous results using the same theoretical method (T-matrix method) under the plane wave illumination. To make comparisons with the published results in Sarkissian et al. (1993), the far-field backscattering amplitude $|A|$ is introduced which has a relationship with the form function (f_∞ in Eq. (30)) by $|f_\infty| = |A| \cdot (kb)$. Panel (a) of Fig. 2 depicts the far-field backscattering amplitude $|A|$ of a rigid fixed (immovable) sphere with the cylindrical portion $h = 0$ (i.e. $l/b = 1$) for end-on ($\theta_i = 0°$) incidence, while panel (b) is for a rigid fixed cylinder with spherical endcaps with half-length $l/b = 2$ under the same condition. The dimensionless frequency kb here is set as the abscissa for the purpose that the computed results are easy to compare with those presented previously in Sarkissian et al. (1993). The incremental step of the dimensionless frequency is set to $\Delta(kb) = 0.02$ for all computations. The surrounding fluid is assumed to be homogeneous, unbounded and inviscid fluid with the sound velocity $c = 1500$m/s and the density $\rho = 1000$kg/m³. The solid lines are calculated using a MATLAB software package based on the present theoretical method, while the circles have been obtained using a commercial software (GetData) for the extraction of data from digital figures. Those correspond to previous results given in Fig. 4 of Sarkissian et al. (1993). As shown in the plots, the numerical results of both the sphere and the finite cylinder with spherical endcaps agree with those of Sarkissian et al. (1993). To further illustrate the effectiveness of the present method for large-aspect-ratio cylinders, other tests for a rigid finite cylinder with an aspect ratio of $l/b = 10$ for both end-on ($\theta_i = 0°$) and broadside ($\theta_i = 90°$) incidences in plane waves are also performed. The corresponding results are displayed in Panels (c) and (d) of Fig. 2, respectively. Here, we set $kL/2$ as the abscissa, so as to correlate the results with those obtained previously (Hackman, 1993), where $L = 2l$ is the total length of the finite cylinder. Again, the results match very well with those given in Fig. 18 (A) of (Hackman, 1993) in the computational frequency bandwidth. Moreover, other tests and comparisons (omitted here for brevity) have been performed and they further demonstrate the correctness and effectiveness of the T-matrix method to calculate the acoustic scattering from rigid finite cylinder with spheroidal endcaps.

Additional tests of convergence have also been performed and the results are plotted in Panels (a) and (b) in Fig. 3. Panel (a) corresponds to the far-field backscattering amplitude $|A|$ for a rigid fixed (immovable) cylinder with spherical endcaps $(d = b)$ having an aspect ratio $l/b = 2$ for $kb = 2$ for end-on ($\theta_i = 0°$) incidence as a function of the maximum truncation index $n_{\max}$. Panel (b) corresponds to the far-field backscattering form function modulus for a rigid fixed (immovable) cylinder with spherical endcaps with $l/b = 10$ for $kL/2 = 10$ for end-on ($\theta_i = 0°$) and broadside ($\theta_i = 90°$) incidence, respectively, as a function of the maximum truncation index $n_{\max}$. In these cases, the half-cone angle is set to $\beta = 30°$. As depicted in Fig. 3, all the results show a fast convergence to the stable solution and the maximum truncation index $n_{\max} = 26$ can adequately ensure the convergence of the results in all the three cases. In order to ensure both the accuracy and computational efficiency, the maximum truncation index $n_{\max} = 25 + \text{Int}(kr_0)$ will be employed in all the following examples, with kr_0 being the dimensionless frequency and r_0 the radius of the circumscribed sphere ($r_0 = l$ for the finite cylinder case). Based on the tests and comparisons described above, the T-matrix method is demonstrated to be effective to calculate the far-field scattering form-function modulus by a rigid fixed (immovable) cylinder with spherical endcaps, even with large aspect ratio
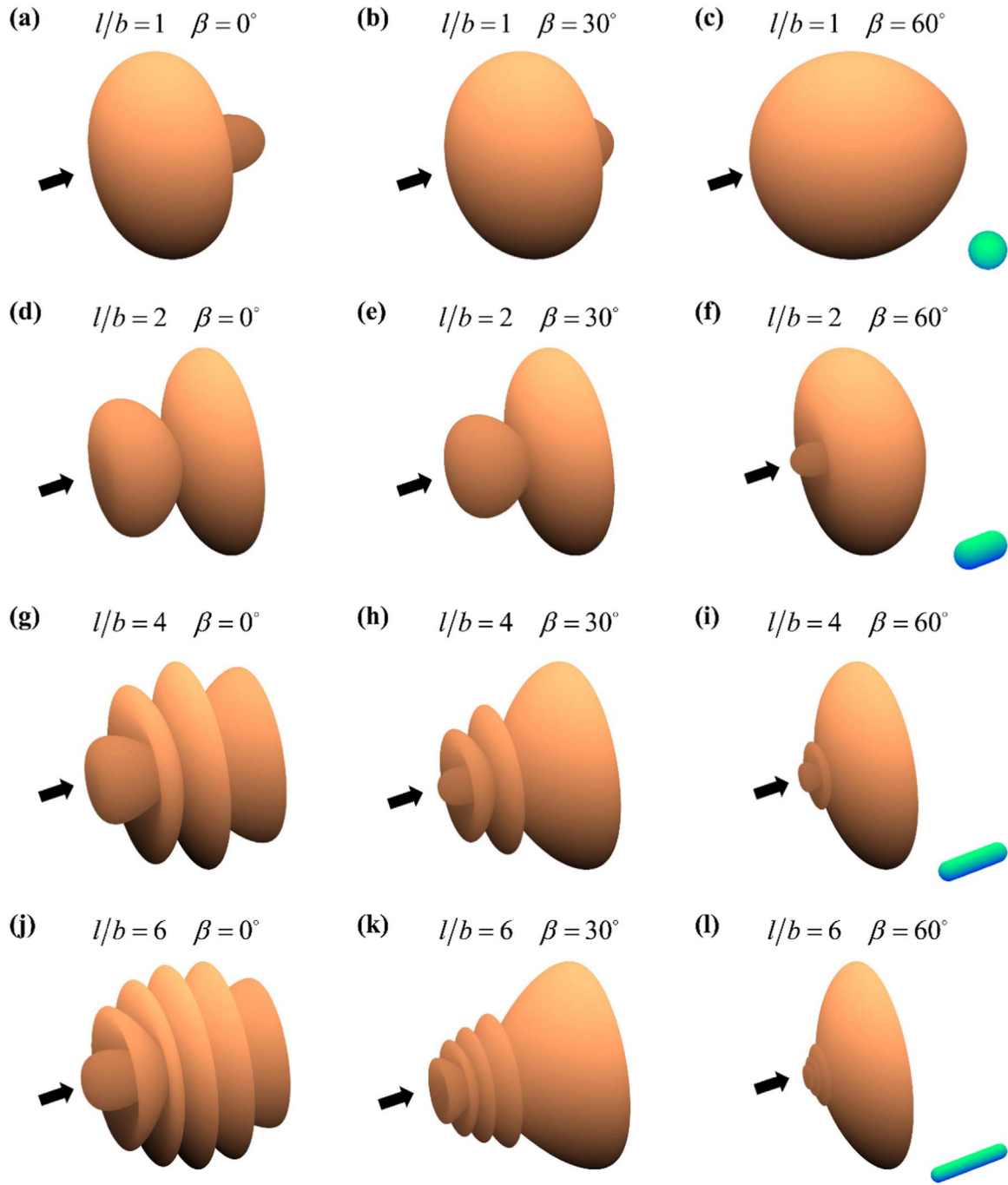
Fig. 7. Panels (a)–(l) display the 3D far-field scattering directivity patterns with end-on ($\theta_i = 0°$) incidence for a rigid fixed (immovable) cylinder with spherical endcaps ($d = b$) in zeroth-order Bessel beam with $l/b = 1$ for panels (a)–(c), $l/b = 2$ for panels (d)–(f), $l/b = 4$ for panels (g)–(i), and $l/b = 6$ for panels (j)–(l), respectively. The parameter $kb = 1.5$ and the half-cone angles$\beta = 0°$, $30°$, and $60°$, corresponding to the three columns, respectively. The arrows on the left-hand side of each panel indicate the direction of incidence of the Bessel beam.

($l/b = 10$). It is anticipated that the present method could be extended to rigid finite cylinder with spheroidal endcaps cases immediately by changing the surface shape function of the considered target accordingly. Here, it is important to note that the present T-matrix method can be even stable to compute acoustic target scattering from elongated aspherical elastic shapes accurately by using Lim's idea (Lim, 2015) based on the approaches proposed recently by Waterman (2009) and Doicu et al. (2000).

3.2. Far-field scattering by the rigid finite cylinder

In this part, a parametric study has been carried out for a rigid finite

cylinder with spheroidal endcaps at end-on incidence ($\theta_i = 0°$) with particular emphasis on varying the half-cone angle, the dimensionless frequency, the aspect ratio of the total length to diameter and the ratio of polar radius to equatorial radius of the spheroidal endcaps. The geometrical model is employed to explain the physical mechanism of the oscillations occurring in the backscattering form function plots of a rigid finite-length cylinder illuminated by a zeroth-order Bessel beam for end-on ($\theta_i = 0°$) incidence.

Panels (a)–(d) of Fig. 4 depict the far-field backscattering form function modulus versus the dimensionless frequency kb with three values of the half-cone angle β of the Bessel beam ($\beta = 0°$ (plane wave case), $30°$, $60°$) at end-on incidence ($\theta_i = 0°$), and the rigid finite cylinder
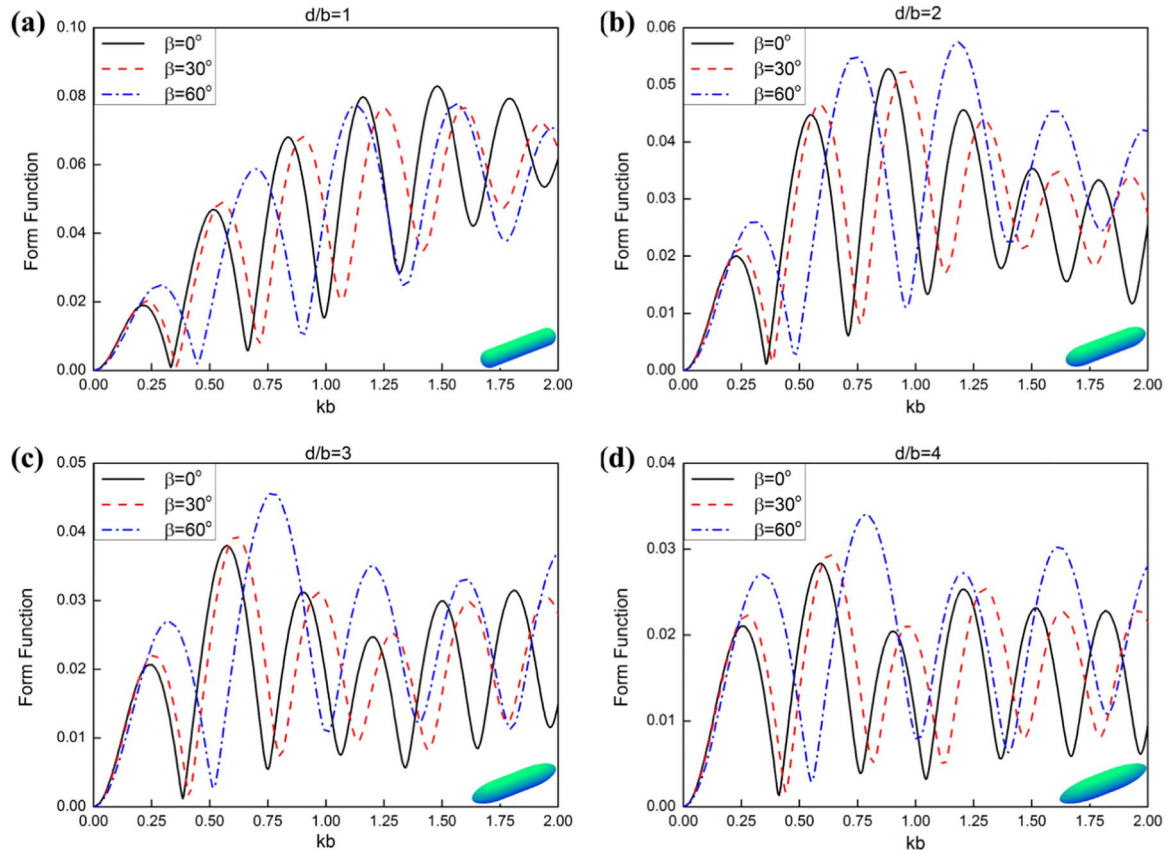
Fig. 8. The far-field backscattering form function modulus at end-on incidence $\theta_i = 0°$ with different half-cone angles β of the Bessel beam versus the dimensionless frequency for a rigid fixed (immovable) cylinder with different-aspect-ratio spheroidal endcaps with $l/b = 5$. Panels (a)–(d) correspond to aspect ratio of spheroidal endcaps of $d/b = 1$, 2, 3 and 4, respectively. The half-cone angles are given explicitly in the legend of each panel.

with spherical endcaps ($d = b$) transforms from a sphere to a highly elongated shape with aspect ratios $l/b = 1$, 2, 4 and 6, respectively. Similarly, the far-field backscattering form function modulus versus the dimensionless frequency kb for broadside ($\theta_i = 90°$) incidence are shown in panels (a)–(d) of Fig. 5, for the same half-cone angle values chosen previously for Fig. 4. As shown in these figures, the quasi-periodic oscillations are observed with the increase of the dimensionless frequency kb for both the end-on and broadside incidences. The physical mechanisms of the quasi-periodic oscillations can be interpreted as the interference between the specular reflection and the Franz waves circumnavigating the rigid finite cylinder in the surrounding fluid. It has also been noticed that for the end-on and broadside incidences in Figs. 4 and 5, the far-field backscattering form function modulus versus dimensionless frequency performs quite differently with respect to the half-cone angle values and aspect ratios. For the end-on incidence in panels (a)–(d) of Fig. 4, the far-field backscattering form function modulus is not sensitive to the half-cone angle values and aspect ratios, while for the broadside incidence in panels (a)–(d) of Fig. 5, quite on the contrary, the modulus is quite sensitive to both the half-cone angle values and aspect ratios except for the sphere case in panel (a) of Fig. 5. Specifically, as observed form panels (b)–(d) of Fig. 5, the far-field backscattering form function modulus decreases as the half-cone angle β increases for the same dimensionless frequency. Also, with the increase of the aspect ratio from $l/b = 1$ to $l/b = 6$ in Fig. 5, the form function modulus increases accordingly.

In addition, the geometrical model (i.e. in terms of acoustical rays) of Bessel beam scattering by a rigid fixed (immovable) cylinder with spheroidal endcaps is employed to compute the peak-to-peak intervals in the backscattering form function, as illustrated in Fig. 6 for the end-on ($\theta_i = 0°$) incidence. In the following, the rigid fixed (immovable) cylinders with spherical endcaps ($d = b$) for end-on ($\theta_i = 0°$) incidence

have taken as examples, which allows to make the corresponding comparisons with the previous results of peak-to-peak intervals in Fig. 4. It is helpful to note the special case when the cylindrical portion $h = 0$, the cylinder with spherical endcaps degenerates to a sphere. The specular points on an impenetrable sphere which can reflect waves parallel or antiparallel to the Bessel beam axis are originally diagramed and discussed (Marston, 2007a). As described in Fig. 6, the specularly reflected wave starts at point A and reflects to the opposite direction of incident beam axis into the water, while the Franz wave propagates along $\overline{BC}$, $\widehat{CD}$ and $\overline{DE}$, and then goes into the surrounding water parallel with the reflection wave. The additional path length of the Franz wave relative to the specular reflection wave can be obtained immediately as

$$\Delta d = \overline{BC} + \widehat{CD} + \overline{DF} \tag{31}$$

By simplifying Eq. (31), the above expression turns into

$$\Delta d = 2b\cos(\beta/2) + 2h + b(\pi - \beta) + 2h\cos\beta \tag{32}$$

Under the assumption that the velocities of the Franz wave and sound in water are the same, the peak-to-peak intervals of the far-field backscattering form function modulus versus the dimensionless frequency can be estimated through the following relation

$$\Delta kb = \frac{2\pi b}{\Delta d} = \frac{2\pi b}{2b\cos(\beta/2) + 2h + b(\pi - \beta) + 2h\cos\beta} \tag{33}$$

It should be noted that similar geometrical formulas can be derived at other angles of incidence considered both for backscattering and bistatic scattering. Table 1 lists the comparison of the peak-to-peak intervals of the far-field backscattering form function modulus versus the dimensionless frequency for a rigid fixed (immovable) cylinder with spherical endcaps ($d = b$) with four values of the aspect ratios
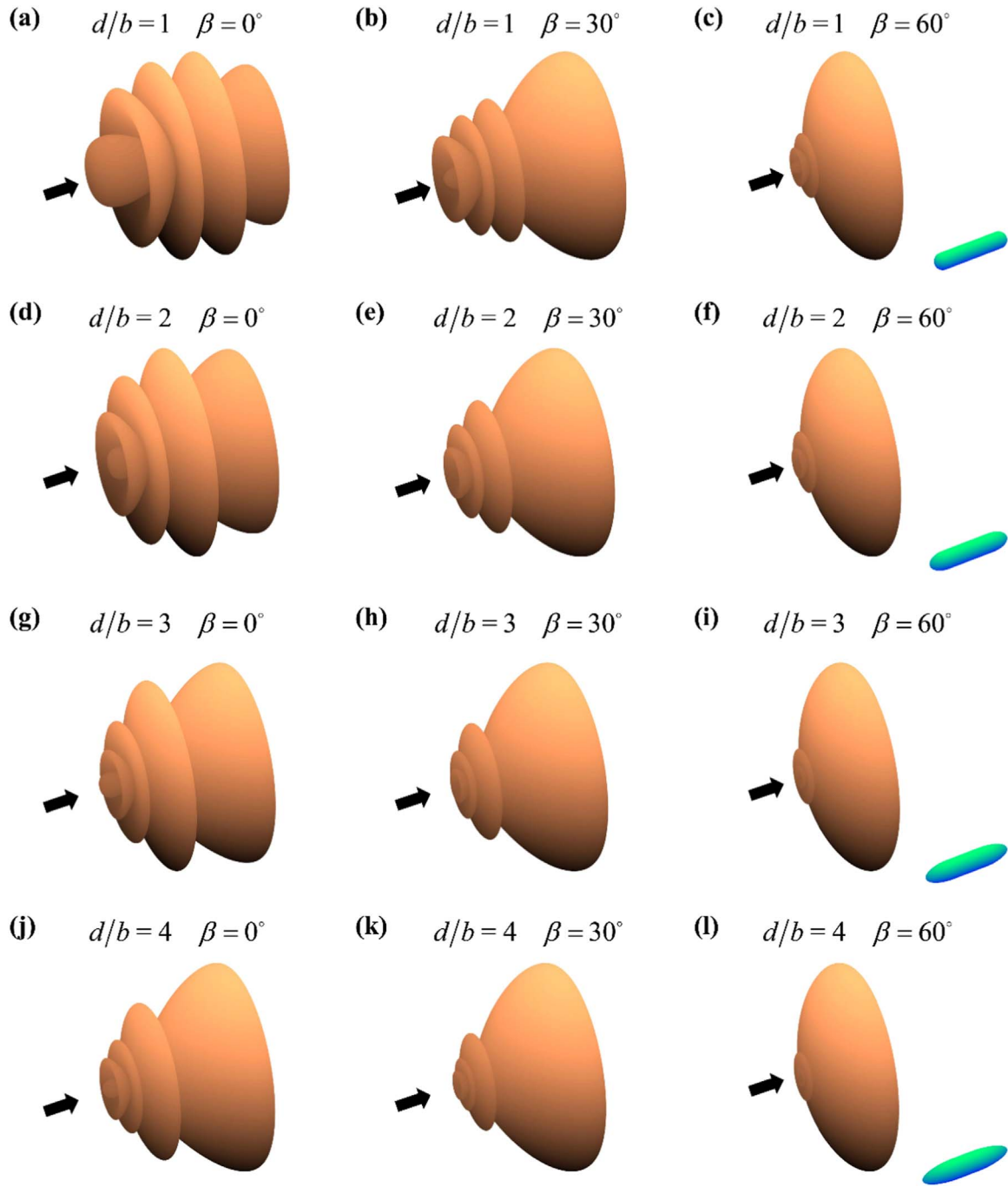
Fig. 9. Panels (a)–(l) display the 3D far-field scattering directivity patterns with end-on ($\theta_i = 0^\circ$) incidence for a rigid fixed (immovable) cylinder, having the aspect ratio of $l/b = 5$, with different-aspect-ratio spheroidal endcaps in zeroth-order Bessel beam with $d/b = 1$ for panels (a)–(c), $d/b = 2$ for panels (d)–(f), $d/b = 3$ for panels (g)–(i), and $d/b = 4$ for panels (j)–(l), respectively. The parameter $kb = 1.5$ and the half-cone angles $\beta = 0^\circ$, 30°, and 60°, corresponding to the three columns, respectively. The arrows on the left-hand side of each panel indicate the direction of incidence of the Bessel beam.

$l/b = 1$, 2, 4, 6, respectively, corresponding to half-cone angles $\beta = 0^\circ$, 30°, 60°. As shown in Table 1, the peak-to-peak intervals predicted by the geometrical model analysis reach a good agreement with the results obtained from Fig. 5. The errors here may be attributed to the assumption that the Franz wave velocity is the same as the sound velocity in water. In fact, the velocity of the Franz wave is slightly lower than the velocity of acoustic wave in water, and is dependent on frequency. In general, it is known that Franz waves tend to give weak scattering contributions to the backscattering because of radiation damping. Noteworthily, a recently discovered situation has been found where the Franz waves actually dominate other scattering mechanisms. The backscattering in water is enhanced by partially-exposed cylinders

at a free surface due to the fact that the Franz wave appears to be partially reflected at the free surface after having been excited on the cylinder by the incident acoustic wave (Eastland and Marston, 2014), however, that case is not under consideration of the present investigation.

To further explore the novel physical phenomenon of acoustic scattering by a rigid fixed (immovable) cylinder under the illumination of a zeroth-order Bessel beam, the 3D far-field scattering directivity patterns at end-on incidence $\theta_i = 0^\circ$ are computed for the same half-cone angles and aspect ratios selected previously as chosen in Fig. 4. Panels (a)–(l) of Fig. 7 display the 3D directivity patterns for a rigid fixed (immovable) cylinder with spherical endcaps ($d = b$) with $l/b = 1$
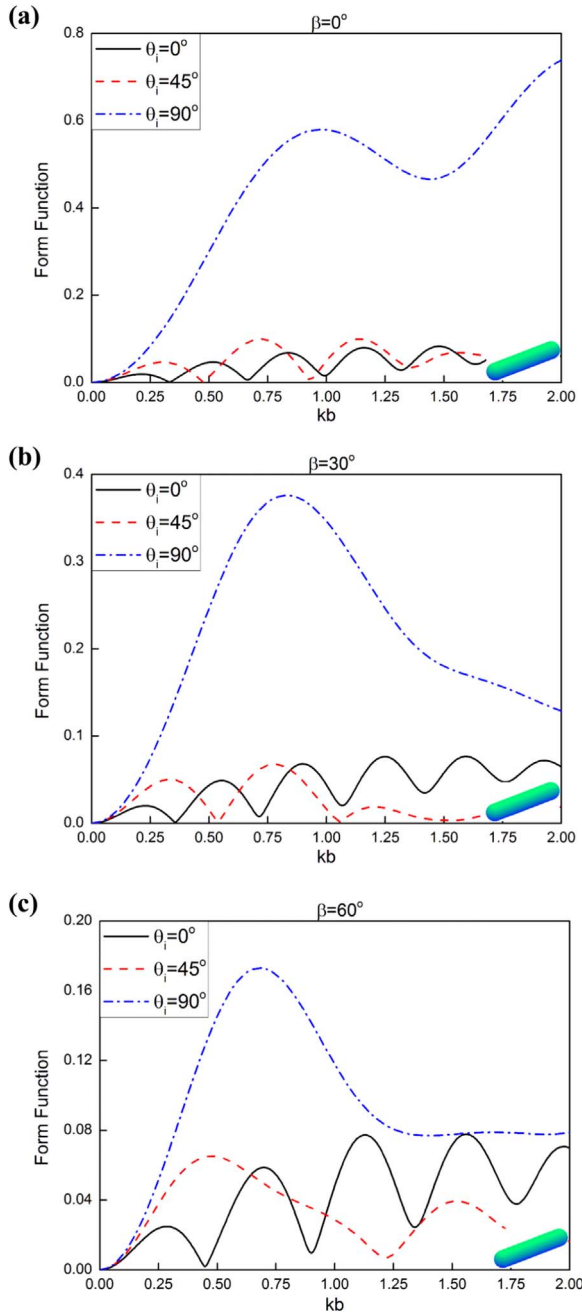
Fig. 10. The far-field backscattering form function modulus at arbitrary angles of incidence [$\theta_i = 0°$ (end-on incidence), $45°$, $90°$ (broadside incidence)] versus the dimensionless frequency for a rigid fixed cylinder with spherical endcaps ($d = b$) with an aspect ratio $l/b = 5$, with different values of the half-cone angle $\beta = 0°$ for panel (a), $\beta = 30°$ for panel (b), and $\beta = 60°$ for panel (c), respectively.

for panels (a)–(c), $l/b = 2$ for panels (d)–(f), $l/b = 4$ for panels (g)–(i) and $l/b = 6$ for panels (j)–(l), respectively. The parameter $kb = 1.5$ and the half-cone angles $\beta = 0°, 30°, 60°$ corresponding to the three columns, respectively, which are given in detail on the top of each panel of Fig. 7. The arrows on the left-hand side of each panel indicate the direction of the incident Bessel beam.

Visual inspection and comparison of the 3D directivity patterns for the finite cylinder with spherical endcaps show significant differences, with particular emphasis on different values of β and aspect ratios. For the cylinder with $h \neq 0$ in panels (d)–(l), it can be observed that the proportion of forward scattering is obviously enhanced as the half-cone angle values increase. Additionally, the number of the lobes in directivity diagrams, as shown in panels (a)–(l) for the same half-cone

angle, increases accordingly when the object turns more slender from a sphere to an elongated cylinder with two spherical endcaps. Moreover, it is interesting to find that the scattering is greatly enhanced in the direction with the scattering angle equal to the half-cone angle, as observed by comparing panels (h) with (i), or panels (k) with (l).

The effect of the aspect ratio of the spheroidal endcaps on the far-field backscattering form function modulus is also discussed in this section. The rigid fixed cylinder with spheroidal endcaps considered here has the aspect ratio of total length to diameter $l/b = 5$. Panels (a)–(d) of Fig. 8 depict the far-field backscattering form function modulus at end-on incidence $\theta_i = 0°$ with three values of the half-cone angle β of the Bessel beam ($\beta = 0°, 30°, 60°$), having the aspect ratio of spheroidal endcaps of $d/b = 1$ for panel (a), $d/b = 2$ for panel (b), $d/b = 3$ for panel (c), and $d/b = 4$ for panel (d), respectively. As observed from these plots, it can be generally concluded that the far-field backscattering form function modulus increases as β increases. Moreover, the far-field backscattering form function modulus is reduced as the spheroidal endcaps become more slender with the aspect ratio from $d/b = 1$ to $d/b = 4$.

Furthermore, the 3D far-field scattering directivity patterns with end-on ($\theta_i = 0°$) incidence for a rigid fixed (immovable) cylinder, having the aspect ratio of $l/b = 5$ with different-aspect-ratio spheroidal endcaps in a zeroth-order Bessel beam with $d/b = 1$ for panels (a)–(c), $d/b = 2$ for panels (d)–(f), $d/b = 3$ for panels (g)–(i), and $d/b = 4$ for panels (j)–(l), respectively, are computed as shown in Fig. 9. The parameter $kb = 1.5$ and the half-cone angles $\beta = 0°, 30°$, and $60°$, corresponding to the three columns, respectively. The arrows on the left-hand side of each panel indicate the direction of incidence of the Bessel beam. Once again, as displayed in Fig. 9 for the cylinder with spheroidal endcaps, the proportion of forward scattering is obviously enhanced as the values of the half-cone angle increase, which is similar to Fig. 7. However, the number of the lobes in directivity diagrams keeps unaltered with the same half-cone angle for different aspect ratios of the spheroidal endcaps, which is quite different from Fig. 7. It should also be noted that the 3D far-field scattering directivity patterns in Fig. 9 show different distribution in the form function modulus, revealing the dependence of the values of half-cone angle and the aspect ratios of the spheroidal endcaps.

3.3. Arbitrary angles of incidence

Several typical angles of incidence are selected, including $\theta_i = 0°$ (end-on incidence), $\theta_i = 45°$, and $\theta_i = 90°$ (broadside incidence), with the same values of the half-cone angle β chosen previously. Panels (a)–(c) in Fig. 10 display the magnitude plots of the far-field backscattering form function versus the dimensionless frequency kb at three values of the incident axial angles θ_i for a rigid fixed cylinder with spherical endcaps ($d = b$) with an aspect ratio $l/b = 5$, and the half-cone angles β are given on the top of each panel, respectively. Generally, for a fixed finite-length cylinder with a specific β as displayed in panels (a)–(c) of Fig. 10, the backscattering form function modulus is enhanced as the incident axial angle increases, particularly in the low-medium frequency bandwidth.

To further investigate the physical mechanism of the scattering by a rigid fixed cylinder with spherical endcaps ($d = b$) in the field of an acoustic zeroth-order Bessel beam with arbitrary orientation, a rigid cylinder with an aspect ratio $l/b = 5$ for $kb = 1.5$ is considered and several 2D polar plots are displayed in panels (a)–(i) of Fig. 11. The polar magnitude plots of the far-field scattering form function with three discrete values of the incident axial angle θ_i are displayed, with the half-cone angles $\beta = 0°$ for panels (a)–(c), $\beta = 30°$ for panels (d)–(f), and $\beta = 60°$ for panels (g)–(i), respectively. As observed, the scattering is enhanced when the scattering angle is equal to the incident axial angle at oblique incidence and this may be attributed to the increase of the specular wave contribution. Moreover, the half-cone angle β also has an influence on the polar patterns and this can be obviously
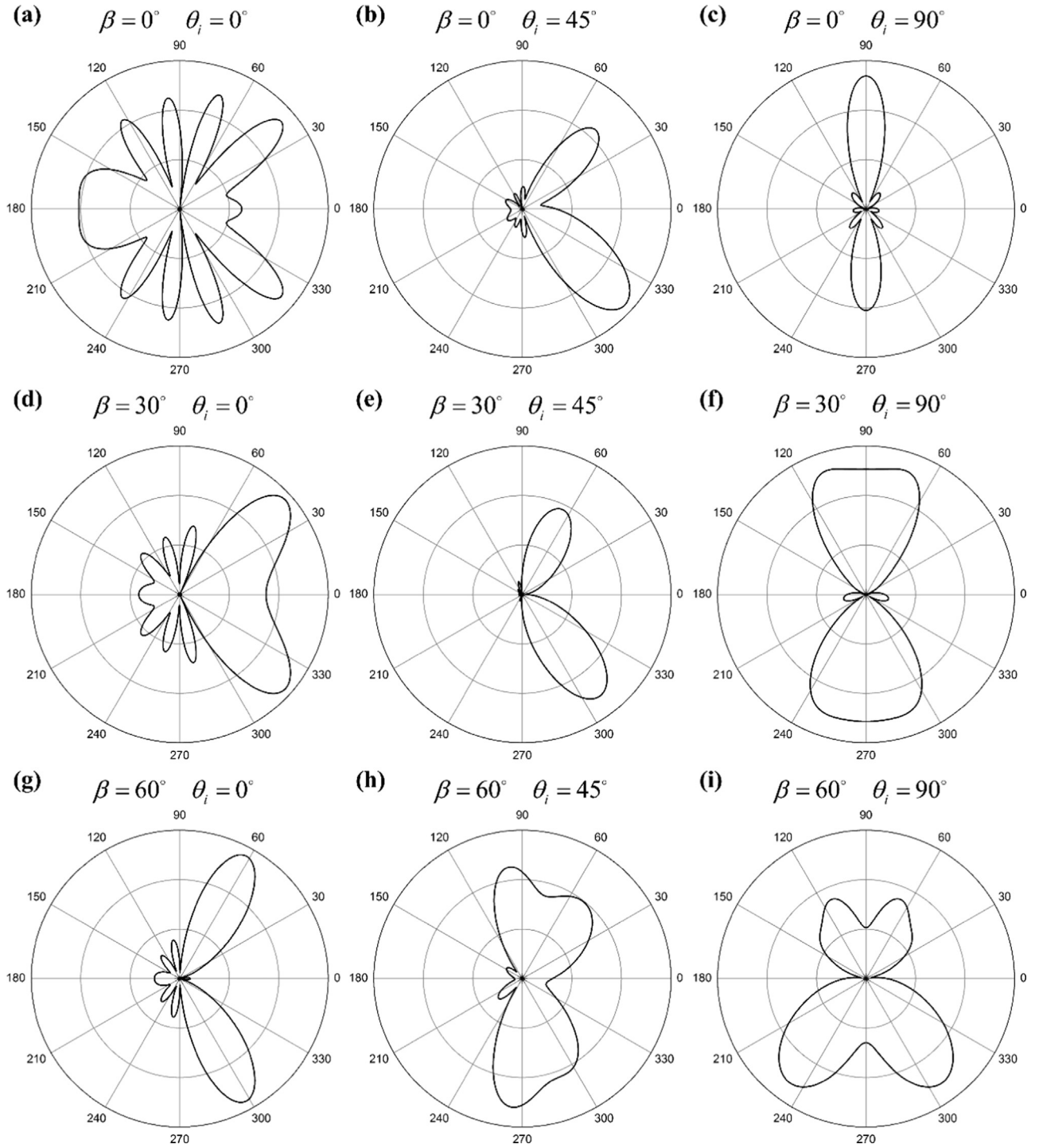
Fig. 11. The 2D polar plots for a rigid fixed cylinder with spherical endcaps ($d = b$) with an aspect ratio $l/b = 5$ for $kb = 1.5$, and the parameters of the incident axial angles θ_i and the values of the half-cone angle β are the same as those used for Fig. 10. The half-cone angles $\beta = 0°$ (panels (a)–(c)), $30°$ (panels (d)–(f)) and $60°$ (panels (g)–(i)), corresponding to the three rows with $\theta_i = 0°$, $45°$ and $90°$, respectively.

observed in panels (d) and (g) for end-on incidence. Furthermore, as shown in the second column (panels (b), (e) and (h)) of Fig. 11, the 2D polar patterns under the oblique incidence show the asymmetry, which are different from those of end-on and broadside incidence cases.

4. Concluding remarks

In the present paper, the theoretical formalism using the T-matrix method to derive and compute the acoustic scattering by a rigid fixed (immovable) finite cylinder with spheroidal endcaps illuminated by an

unbounded zeroth-order Bessel beam with arbitrary incidence is established. The proposed method is demonstrated to be capable of computing accurately the scattered field of finite cylinder with spheroidal endcaps, even having an aspect ratio of $l/b = 10$ at arbitrary orientation. Based on the theoretical formulation derived above, a MATLAB software package is developed and tested. It is proved to be an effective numerical tool to tackle scattering problems for finite-length cylinder with spheroidal endcaps, in the field of a zeroth-order Bessel beam. Numerical computations are performed with particular emphasis on the half-cone angle β of the Bessel beam, the dimension-

less frequency, the aspect ratios (including the ratio of total length to diameter of the finite cylinder and the ratio of polar radius to equatorial radius of the spheroidal endcaps), as well as the angle of incidence θ_i. Furthermore, the geometrical model based on the interference between the specular reflection wave and the Franz wave is employed to calculate the peak-to-peak intervals of dimensionless frequency and can further demonstrate the effectiveness of the *T*-matrix method for acoustical Bessel beam scattering problems. When encountering scattering problems by obstacles having complex geometries under the illumination of an acoustical Bessel beam, the *T*-matrix method presents a useful and valuable tool along that direction of research.

Acknowledgements

References

Anderson, V.C., 1950. Sound scattering from a fluid sphere. J. Acoust. Soc. Am. 22, 426–431.

Bouchal, Z., 2003. Nondiffracting optical beams: physical properties, experiments, and applications, Czechoslovak. J. Phys. 53, 537–578.

Bouchal, Z., Wagner, J., Chlup, M., 1998. Self-reconstruction of a distorted nondiffracting beam. Opt. Commun. 151, 207–211.

Doicu, A., Eremin, Y., Wriedt, T., 2000. Acoustic and Electromagnetic Scattering Analysis using Discrete Sources. Academic Press, New York.

Durnin, J., Miceli, J., Eberly, J.H., 1987. Diffraction-free beams. Phys. Rev. Lett. 58, 1499–1501.

Eastland, G.C., Marston, P.L., 2014. Enhanced backscattering in water by partially-exposed cylinders at free surfaces associated with an acoustic Franz wave. J. Acoust. Soc. Am. 135, 2489–2492.

Fahrbach, F.O., Simon, P., Rohrbach, A., 2010. Microscopy with self-reconstructing beams. Nat. Photonics 4, 780–785.

Faran, J.J., 1951. Sound scattering by solid cylinders and spheres. J. Acoust. Soc. Am. 23, 405–418.

Freedman, A., 1962. A mechanism of acoustic echo formation. Acta Acust. United Acust. 12, 10–21.

Garces-Chavez, V., McGloin, D., Melville, H., Sibbett, W., Dholakia, K., 2002. Simultaneous micromanipulation in multiple planes using a self-reconstructing light beam. Nature 419, 145–147.

Gaunaurd, G.C., 1985. Sonar cross sections of bodies partially insonified by finite sound beams. IEEE J. Ocean. Eng. 10, 213–230.

Gaunaurd, G.C., Überall, H., 1983. RST analysis of monostatic and bistatic acoustic echoes from an elastic sphere. J. Acoust. Soc. Am. 73, 1–12.

Green, L.H., 1987. Acoustic resonance scattering by large aspect-ratio solid targets. IEEE J. Ocean. Eng. 81, 368–379.

Hackman, R.H., 1993. Acoustic Scattering From Elastic Solids in Physical Acoustics XXII. Academic Press, Boston, Massachusetts.

Hackman, R.H., Todoroff, D.G., 1985. An application of the spheroidal-coordinate-based transition matrix: the acoustic scattering from high aspect ratio solids. J. Acoust. Soc. Am. 78, 1058–1071.

Hickling, R., 1958. Frequency dependence of echoes from bodies of different shapes. J. Acoust. Soc. Am. 30, 137–139.

Jansson, P.A., 1993. Acoustic scattering from a rough sphere. J. Acoust. Soc. Am. 93, 3032–3042.

Junger, M.C., 1982. Scattering by slender bodies of revolution. J. Acoust. Soc. Am. 72, 1954–1956.

Keller, J.B., Ahluwalia, D.S., 1971. Diffraction by a curved wire. SIAM J. Appl. Math. 20, 390–405.

Lax, M., Feshbach, H., 1948. Absorption and scattering for impedance boundary conditions on spheres and circular cylinders. J. Acoust. Soc. Am. 20, 108–124.

Li, W., Li, J., 2012. Underwater acoustic scattering of a Bessel beam by rigid objects with arbitrary shapes using the T-matrix method. In: Proceedings of the OCEANS'12 MTS/IEEE, Hampton Roads, Virginia, October, pp. 1–5.

Li, W., Li, J., Gong, Z.X., 2015. Study on underwater acoustic scattering of a Bessel beam by rigid objects with arbitrary shapes. Acta Phys. Sin. 64. http://dx.doi.org/10.7498/aps.64.154305.

Lim, R., 2015. A more stable transition matrix for acoustic target scattering by elongated objects. J. Acoust. Soc. Am. 138, 2266–2278.

Liu, S.G., Gong, Z.X., Chai, Y.B., Li, W., 2016. Underwater acoustic scattering of Bessel beam by spherical shell using T-matrix method. In: Proceedings of the IEEE/OES China Ocean Acoustics Symposium, Harbin, China, January, pp. 1–6.

López-Mariscal, C., Gutiérrez-Vega, J.C., 2007. The generation of nondiffracting beams using inexpensive computer-generated holograms. Am. J. Phys. 75, 36–42.

Marston, P.L., 2006. Axial radiation force of a Bessel beam on a sphere and direction reversal of the force. J. Acoust. Soc. Am. 120, 3518–3524.

Marston, P.L., 2007a. Scattering of a Bessel beam by a sphere. J. Acoust. Soc. Am. 121,

753–758.

Marston, P.L., 2007b. Acoustic beam scattering and excitation of sphere resonance: bessel beam example. J. Acoust. Soc. Am. 122, 247–252.

Marston, P.L., 2007c. Negative axial radiation forces on solid spheres and shells in a Bessel beam. J. Acoust. Soc. Am. 122, 3162–3165.

Marston, P.L., 2008. Scattering of a Bessel beam by a sphere: II. helicoidal case and spherical shell example. J. Acoust. Soc. Am. 124, 2905–2910.

Marston, P.L., 2009. Radiation force of a helicoidal Bessel beam on a sphere. J. Acoust. Soc. Am. 125, 3539–3547.

Marston, P.L., Wei, W., Thiessen, D.B., 2006. Acoustic radiation force on elliptical and spheroidal objects in low frequency standing waves. In: Proceedings of the AIP Conference, 838, pp. 495-499, http://dx.doi.org/10.1063/1.2210403.

Mitri, F.G., 2008a. Acoustic radiation force on a sphere in standing and quasi-standing zero-order Bessel beam tweezers. Ann. Phys. 323, 1604–1620.

Mitri, F.G., 2008b. Acoustic scattering of a high-order bessel beam by an elastic sphere. Ann. Phys. 323, 2840–2850.

Mitri, F.G., 2009a. Langevin acoustic radiation force of a high-order bessel beam on a rigid sphere. IEEE Trans. Ultrason. Ferroelectr. Freq. Control 56, 1059–1064.

Mitri, F.G., 2009b. Equivalence of expressions for the acoustic scattering of a progressive high-order bessel beam by an elastic sphere. IEEE Trans. Ultrason. Ferroelectr. Freq. Control 56, 1100–1103.

Mitri, F.G., 2009c. Negative axial radiation force on a fluid and elastic spheres illuminated by a high-order Bessel beam of progressive waves. J. Phys. A: Math. Theor. 42, 245202.

Mitri, F.G., 2010. Interaction of a high-order Bessel beam with a submerged spherical ultrasound contrast agent shell–scattering theory. Ultrasonics 50, 387–396.

Mitri, F.G., 2011. Acoustic beam interaction with a rigid sphere: the case of a first-order non-diffracting Bessel trigonometric beam. J. Sound Vib. 330, 6053–6060.

Mitri, F.G., 2015a. Acoustic scattering of a Bessel vortex beam by a rigid fixed spheroid. Ann. Phys. 363, 262–274.

Mitri, F.G., 2015b. Axisymmetric scattering of an acoustical bessel beam by a rigid fixed spheroid. IEEE Trans. Ultrason. Ferroelectr. Freq. Control 62, 1809–1818.

Mitri, F.G., 2015c. Acoustic radiation force on oblate and prolate spheroids in Bessel beams. Wave Motion 57, 231–238.

Mitri, F.G., Fellah, Z.E.A., 2011. Instantaneous axial force of a high-order Bessel vortex beam of acoustic waves incident upon a rigid movable sphere. Ultrasonics 51, 719–724.

Mitri, F.G., Silva, G.T., 2011. Off-axial acoustic scattering of a high-order Bessel vortex beam by a rigid sphere. Wave Motion 48, 392–400.

Narayanan, M.S., Garg, D.D., 1968. High frequency acoustic scattering form ellipsoids and cylinders. IETE J. Res. 14, 239–248.

Peterson, B., Ström, S., 1974. Matrix formulation of acoustic scattering from an arbitrary number of scatterers. J. Acoust. Soc. Am. 56, 771–780.

Piestun, R., Shamir, J., 1998. Generalized propagation-invariant wave fields. J. Opt. Soc. Am. A 15, 3039–3044.

Rayleigh, L., 1945. The Theory of Sound, Dover, New York.

Rumerman, M.L., 1992. Application of the Sommerfeld–Watson transformation to scattering of acoustic waves obliquely incident upon cylindrical shells. J. Acoust. Soc. Am. 91, 2502–2509.

Sarkissian, A., Gaumond, C.F., Dragonette, L.R., 1993. T-matrix implementation of forward scattering from rigid structures. J. Acoust. Soc. Am. 94, 3448–3453.

Schenck, H.A., 1968. Improved integral formulation for acoustic radiation problems. J. Acoust. Soc. Am. 44, 41–58.

Silva, G.T., 2011. Off-axis scattering of an ultrasound bessel beam by a sphere. IEEE Trans. Ultrason. Ferroelectr. Freq. Control 58, 298–304.

Silva, G.T., Lopes, J.H., Mitri, F.G., 2013. Off-axial acoustic radiation force of repulsor and tractor bessel beams on a sphere. IEEE Trans. Ultrason. Ferroelectr. Freq. Control 60, 1207–1212.

Stanton, T.K., 1988. Sound scattering by cylinders of finite length. I. fluid cylinders. J. Acoust. Soc. Am. 83, 55–63.

Stratton, J.A., 2007. Electromagnetic Theory. John Wiley & Sons, Hoboken, New Jersey.

Su, J.H., Varadan, V.V., Varadan, V.K., Flax, L., 1980. Acoustic wave scattering by a finite elastic cylinder in water. J. Acoust. Soc. Am. 68, 686–691.

Van Nhieu, M.T., Ywanne, F., 1994. Sound scattering by slender bodies of arbitrary shape. J. Acoust. Soc. Am. 95, 1726–1733.

Varadan, V.K., yaradan, V.V., 1980. Acoustic, Electromagnetic and Elastic Wave Scattering–Focus on the T-matrix Approach. Pergamon, New York.

Varadan, V.K., Varadan, V.V., Dragonette, L.R., Flax, L., 1982. Computation of rigid body scattering by prolate spheroids using the T-matrix approach. J. Acoust. Soc. Am. 71, 22–25.

Varadan, V.V., 1978. Scattering matrix for elastic waves. II. Application to elliptic cylinders. J. Acoust. Soc. Am. 63, 1014–1024.

Varadan, V.V., Varadan, V.K., 1987 Multiple Scattering of Waves in Random Media and Random Rough Surfaces, Technomic Publishing Company.

Varadan, V.V., Lakhtakia, A., Varadan, V.K., 1991. Field Representations and Introduction to Scattering. Elsevier Science Publishing Company, North-Holland.

Waterman, P.C., 1965. Matrix formulation of electromagnetic scattering. Proc. IEEE 53, 805–812.

Waterman, P.C., 1969. New formulation of acoustic scattering. J. Acoust. Soc. Am. 45, 1417–1429.

Waterman, P.C., 2009. T-matrix methods in acoustic scattering. J. Acoust. Soc. Am. 125, 42–51.

Ye, Z., 1997. A novel approach to sound scattering by cylinders of finite length. J. Acoust. Soc. Am. 102, 877–884.

Zhang, L., Marston, P.L., 2011. Geometrical interpretation of negative radiation forces of acoustical Bessel beams on spheres. Phys. Rev. E 84, 035601.

Zhang, L., Marston, P.L., 2012. Axial radiation force exerted by general non-diffracting beams. J. Acoust. Soc. Am. 131, EL329–EL335.